Chinese Chemical Letters 34 (2023) 107545

Contents lists available at ScienceDirect

Chinese Chemical Letters

journal homepage: www.elsevier.com/locate/cclet

V-substituted pyrochlore-type polyantimonic acid for highly enhanced lithium-ion storage

Haoyu Fang, Kai Yong, Boya Wang, Kaipeng Wu*, Yun Zhang, Hao Wu*

College of Materials Science and Engineering, Sichuan University, Chengdu 610064, China

ARTICLE INFO

Article history:
Received 26 April 2022
Revised 10 May 2022
Accepted 18 May 2022
Available online 23 May 2022

Keywords:
Lithium-ion batteries
Anode materials
Polyantimonic acid
Element substitution
Electrochemical reaction mechanism

ABSTRACT

Pyrochlore-structured polyantimonic acid (PAA) is a potential high-capacity electrode material, but its innately poor electroconductivity ($\sim10^{-10}$ S/cm) seriously impairs its electrochemical reversibility for lithium-ion storage. Herein, we report design and synthesis of a novel V-substituted PAA (PAA-V), where V^{5+} are introduced to partially replace Sb^{5+}. Owing to identical valence and close ionic radius relative to Sb^{5+}, the V^{5+} cation can constitute the covalent VO_6 octahedra framework without changing the pyrochlore crystal structure of PAA. As a result, the V^{5+}-substitution is capable to modulate the electronic structure of PAA with significantly improved electrical conductivity ($\sim10^{-6}$ S/cm for PAA-V) and meanwhile decreases the size of crystals with reduced diffusion length for Li^+-ions. With varying the ratio of V^{5+}-substitution, the PAA-V with optimized substitution molar ratio (18%) exhibits the best lithium-ion storage performance, delivering a long cycling life with high reversible capacity (731 mAh/g after 1200 cycles at 1 A/g) and outstanding rate capability (279 mAh/g at 15 A/g). More importantly, by pairing the PAA-V as anode and commercial $LiFePO_4$ as cathode, the full cell with a limited negative/positive capacity ratio of 1.2 exhibits decent cycling stability at 1 C after 150 cycles with 85.5% capacity retention.

With the rapid development of various portable electronic devices and inevitable electrification of transportation vehicles, the demand for rechargeable lithium-ion batteries (LIBs) with high specific capacity and good stability continues to grow [1,2]. Electrodes as an important part in LIBs essentially determine the electrochemical performance of LIBs. Graphite is the most common anode electrodes used in current LIBs, but it only provides a relatively low specific capacity (372 mAh/g) and poor rate performance [3,4]. Antimony-based materials including metallic Sb, Sb-base alloys, Sb oxides, and Sb-O based compounds are considered to be promising anode materials for high-capacity LIBs owing to their high theoretical capacity (>660 mAh/g), suitable working potential (0.6–0.9 V *vs.* Li^+/Li), environmental benign, and abundance [5,6]. Polyantimonic acid (PAA, $(H_3O)_pH_{2-p}Sb_2O_6$) is a pentavalent antimony compound with a unique pyrochlore crystal structure comprising corner-sharing SbO_6 octahedra and three-dimensional accessible open channels [7,8]. This tunnel-like structure benefits fast proton mobility (10^{-3}-10^{-4} S/cm) and transmission of various metal cations, and thus making the PAA a superior inorganic ion exchanger [9,10]. Additionally, the PAA containing pentavalent Sb^{5+} species could deliver high theoretical specific capacity, like Sb_2O_3 (1109 mAh/g) with Sb^{3+} and Sb_6O_{13} (1270 mAh/g) with Sb^{3+}/Sb^{5+} [11,12]. However, the innately terrible bulk electronic conductivity of PAA ($\sim10^{-10}$ S/cm) considerably impairs its electrochemical reversibility, hence hindering the application in LIBs.

Coating with high conductive carbon materials and element doping/substitution are two feasible methods to improve the electronic structure of various inorganic materials [13–16], which have been also applied to enhance the inherently ultralow electronic conductivity of PAA as well as its electrochemical reversibility for lithium-ion storage, as performed in previous reports by our group [17,18]. However, the coating method only improving the electronic conductivity for the surface of PAA with unimproved bulk electronic conductivity. Besides, the conductive carbon coating materials comsume more electrolyte and also lead to low density with inferior volumetric capacity. Thus, the element doping/substitution method without these disadvantages should be studied in depth. In consideration of the pyrochlore crystal structure, element doping/substitution can be employed to two atomic sites in PAA, one is doping in the open tunnels [19], and the other is replacing the Sb^{5+} in the center of SbO_6 octahedra [20]. Most recently, we reported an element substitution tactics to tune the electronic structure of PAA [18]. A small amount of Mn^{2+} was introduced for partial substitution over the H_3O^+ in the tunnel cavities in PAA, which not only narrows the bandgap to increase its intrinsic electronic

* Corresponding authors.
E-mail addresses: wukaipeng@scu.edu.cn (K. Wu), hao.wu@scu.edu.cn (H. Wu).

https://doi.org/10.1016/j.cclet.2022.05.059
1001-8417/

conductivity, but also reduces the lithium-ion migration energy barrier. However, the studies *via* element substitution by replacing the Sb^{5+} has not been reported so far, meanwhile the effect on improving the electrochemical properties of PAA still remains unknown.

In this work, we successfully synthesized V^{5+}-substituted PAA (PAA-V) by a simple one-pot hydrothermal way, where V^{5+} partially replacing Sb^{5+} in the center of SbO_6 octahedra. V^{5+} and Sb^{5+} have the same charge with identical coordination number of 6, meanwhile the ionic radius size of V^{5+} (0.054 nm) is close to that of Sb^{5+} (0.060 nm) [21]. Accordingly, the V^{5+} cations can successfully replace the Sb^{5+} in as-prepared PAA-V, while maintaining the pyrochlore crystal structure with 3D open channels for rapid ionic migration. The partial substitution of Sb^{5+} by V^{5+} not only decease the size of crystals to nanoscale, but also modulate the electronic structure of PAA. Moreover, the V^{5+} in PAA-V only occurs conversion reaction to *in-situ* form metallic V^0 during discharge/charge process, which further raises the charge transfer kinetics of electrodes [22,23]. Furthermore, the PAA-V with optimized V^{5+}-substituted molar ratio (18%) was also synthesized as it exhibits the highest electrical conductivity and the best particle dispersibility. As a result, thus-optimized PAA-V sample as the anode material shows the best electrochemical performance including long cycling life (731 mAh/g after 1200 cycles at 1 A/g), outstanding rate capability (279 mAh/g at 15 A/g), and good compatibility with commercial cathodes even at controlled negative/positive capacity (N/P) ratio (≈1.2), and hence has potential in application of high-capacity anode of LIBs.

The synthesis process of the PAA-V is shown in Fig. 1a, which shows a facile one-pot hydrothermal reaction. Specifically, potassium hexahydroantimonate (V) ($KSb(OH)_6$, CAS No. 12208-13-8) and sodium metavanadate ($NaVO_3{\cdot}2H_2O$, CAS No. 13718-26-8) were used as the Sb^{5+} and V^{5+} sources, respectively. $KSb(OH)_6$ and $NaVO_3{\cdot}2H_2O$ with a certain molar ratio were added into 37 mL deionized water. Then the suspension was heated to 80 °C with stirring for 10 min, until the suspension turned into transparent solution. After that, 23 mL CH_3OH was added into the above-obtained solution, which was then transferred to a 100 mL Teflon-lined autoclave and placed in an oven at 170 °C for 12 h. When cooled down to room temperature naturally, the light yellow PAA-V precipitates were collected by filtration and washed with distilled water and ethanol, and finally dried in air at 60 °C. The pristine PAA was also produced by the same method without the addition of V^{5+} source. For the purpose of optimizing the structure and electrochemical performance of PAA-V with different V^{5+}-substitution ratio, we synthesized five kinds of PAA-V samples, named as PAA-$V_{\#1}$, PAA-$V_{\#2}$, PAA-$V_{\#3}$, PAA-$V_{\#4}$, and PAA-$V_{\#5}$, by adjusting the molar ratio of $KSb(OH)_6$ and $NaVO_3{\cdot}2H_2O$. The specific molar ratios of the two reagents are listed in Table S1 (Supporting information).

The structure and crystalline phase analyses were conducted by X-ray diffraction (XRD, Philips X'pert TROMPD, Cu Kα radiation, $\lambda = 1.54178$ Å). The surface elemental compositions and their valences in the samples were measured by X-ray photoelectron spectroscopy (XPS, Escalab 250, Thermo Fischer Scientific, USA). The morphology and microstructure of the samples were examined by a field emission scanning electron microscopy (SEM, Hitachi, S-4800, Japan) and a transmission electron microscopy (TEM, FEI, Titan themis 200, USA). The compositions were analyzed by the energy dispersive X-ray spectroscopy (EDS). The contents of metal ions were tested by inductively coupled plasma optical emission spectroscopy (ICP-OES, AVIO 200, USA). Particle sizes were tested by DLS measurements by Zetasizer Nano ZS90. Nitrogen adsorption/desorption isotherms and pore size distributions were characterized using a Kubo-X1000 analyzer (Beijing Builder Electronic Technology Co., Ltd.). The specific surface areas and pore size distribution were derived by Brunauer-Emmett-Teller (BET) and Barrett-Joyner-Halenda (BJH) methods, respectively. The thermogravimetry analysis was conducted by Shimadzu DTG-60H (Shimadzu, Japan). Raman spectra were recorded on a Raman spectrophotometer (Horiba Jobin Yvon, HR800, France) with 532 nm laser radiation. The electrical conductivity of samples was measured by four-probe method by a semiconductor powder resistivity tester (ST-2722). UV-vis diffused reflectance spectrum (UV-vis DRS) were tested by an UV-vis spectrometer (Shimadzu, UV3600, Japan).

To assess the electrochemical performances of the PAA-V as anodes for lithium-ion batteries, CR2032 coin-type half cells were assembled in an argon-filled glove box using lithium metal as the counter electrode and commercial membrane (Celgard 2400) as

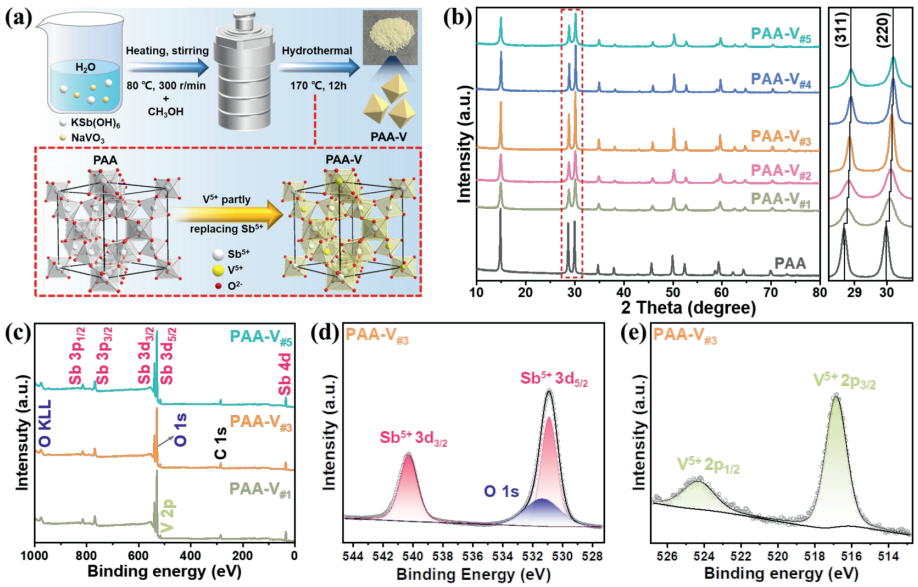

Fig. 1. (a) Schematic illustration of the synthesis process for the PAA-V. (b) XRD spectra of the PAA and PAA-$V_{\#1\text{-}5}$. (c) XPS survey spectra of the PAA-$V_{\#1}$, PAA-$V_{\#3}$ and PAA-$V_{\#5}$. High-resolution spectra of (d) Sb 3d and (e) V 2p of the PAA-$V_{\#3}$.

the separator. The anodes were prepared by the following procedures. Typically, the anode slurry was prepared by mixing active materials, conducting agent (Ketjen black), and binder (carboxymethyl cellulose) in deionized water solvent dispersant in a weight ratio of 7:2:1, and then coated on Cu foil and dried at 60 °C in vacuum for 12 h. The mass of the active materials was kept at ≈1 mg/cm^2. The final foil was punched into disk with a diameter of 12 mm as the working electrode. The electrolyte is consisted of a solution of 1.0 mol/L $LiPF_6$ solution in a mixture of ethylene carbonate, ethylmethyl carbonate, and dimethyl carbonate (EC/DMC/DEC, 1:1:1, v/v/v) with 5% fluoroethylene Carbonate (FEC). The galvanostatic discharge and charge performance were measured by an automatic NEWARE battery cycler (CT-4008T-5V-20/50mA, Shenzhen, China) in a voltage range of 0.01–3.0 V at room temperature. Galvanostatic intermittent titration technique (GITT) measurements were performed by using the automatic NEWARE battery cycler with a pulse current of 100 mA/g applied for 30 min. After each pulse, the cells rested for 1 h to reach the equilibrium potential. Cyclic voltammetry (CV) curves were tested between 0.01 V and 3.0 V. Electrochemical impedance spectra (EIS) were acquired in the frequency range from 100 Hz to 0.1 Hz at an AC voltage of 5 mV. The CV and EIS measurements were both carried out on a PARSTAT multichannel electrochemical workstation (Princeton Applied Research, PMC1000, USA).

For the coin full cells, the commercial $LiFePO_4$ (LFP, 1 C = 160 mA/g) was adopted as cathode material. The cathode electrodes composing of LFP (80 wt%), Ketjen black (15 wt%), and polyvinylidene fluoride (5 wt%) coated on Al foil were dried at 80 °C in vacuum for 12 h. To avoid the large irreversible capacity loss in the initial cycle, the PAA-V electrodes were firstly pre-cycled in the abovementioned half cells before using in the full cells [24,25]. Then, the PAA-V//LFP lithium-ion full cells were assembled by the as-prepared LFP cathode and pre-cycled PAA-V anode with controlled negative/positive capacity ratio (N/P) of 1.2. The rate and cycling performance of the PAA-V//LFP full cells were performed in a voltage range of 1.0−3.5 V using the automatic NEWARE battery cycler.

First of all, the distinctive appearance difference between PAA and PAA-$V_{\#1\text{-}5}$ can be identified from their photographs as shown in Fig. S1 (Supporting information). PAA exhibits the appearance of white powder, but PAA-$V_{\#1\text{-}5}$ are all light yellow, reflecting that the microstructure and elemental compositions of PAA-$V_{\#1\text{-}5}$ are obviously different from those of PAA. XRD was then performed for each sample to identify the phase purity and crystal structure. As shown in Fig. 1b, all the diffraction peaks for PAA-$V_{\#1\text{-}5}$ can be well assigned to the cubic pyrochlore-type crystallographic structure, evidencing that the PAA-V samples have the identical crystal framework with space group symmetry of $Fd\overline{3}m$ as the PAA. This implies that the V^{5+}-substitution does not lead to a transformation of the pyrochlore structure of PAA. However, the shape and strength of the diffraction peaks of PAA-$V_{\#1\text{-}5}$ samples have certain variance with each other, indicating that the crystallinity and grain size of them have difference. For PAA-$V_{\#1}$ and PAA-$V_{\#2}$ samples, the relatively larger values of the full width at half maxima (FWHM) of their diffraction peaks suggest smaller grain sizes. For PAA-$V_{\#4}$ and PAA-$V_{\#5}$ samples, the strength of their diffraction peaks gradually reduces, suggesting that the crystallinity of the two samples progressively could be reduced. Note that, the sharp diffraction peaks of PAA-$V_{\#3}$ sample indicate its high crystallinity and phase purity. Simultaneously, the position of reflection peaks gradually shift to higher 2θ values for the PAA-V samples as the V^{5+}-substitution ratio become higher, which is associated with the lattice contraction. Such alteration is further elucidated in the inset of Fig. 1b, which magnifies the (311) and (220) diffraction peaks. Besides, the positions of diffraction peaks of PAA-$V_{\#4}$ and PAA-$V_{\#5}$ samples are almost the same, indicating that the V^{5+}-substitution ratio could reach the maximum for the two samples with identical lattice parameter. The decrease of the unit cell volume may be ascribed to substitution of Sb^{5+} by V^{5+}, because the ionic size of V^{5+} is slightly smaller than that of Sb^{5+}, $r(V^{5+}) = 0.054$ nm and $r(Sb^{5+}) = 0.060$ nm [21]. Therefore, with the content of V^{5+} in PAA-V increasing, the unit cell volume turns smaller.

Generally speaking, PAA with the pyrochlore-type lattice cell has four atomic occupancy positions, *i.e.*, 16c, 48f, 16d and 8b sites. To be specific, the 16c sites (0, 0, 0) are occupied by Sb^{5+} ions in the centers of SbO_6 octahedra, and the 48f sites (x, 1/8, 1/8) include O^{2-} at the apices of the SbO_6 octahedra [26]. These corner-shared SbO_6 octahedra build a three-dimensional accessible tunnel-like framework with large-sized cavities, signed as 16d and 8b site containing H^+/H_3O^+ [20,27]. In theory, since the V^{5+} and Sb^{5+} have same positive charge of 5 and identical coordination number of 6, together with similar ionic radii size. Hence, it is reasonable that the V^{5+} ions would occupy at the 16c sites by replacing the Sb^{5+} ions in PAA-V samples. To confirm the validity of such structure, XRD Rietveld refinement was subsequently carried out. Because the reliability of result of the XRD refinement is highly depend on the quality of powder XRD data, we chose to conduct Rietveld refinement on the basis of powder XRD data of PAA-$V_{\#3}$ sample, which has the sharpest reflection peaks. As a comparison, the XRD data of pristine PAA was also analyzed by Rietveld refinement. As expected, the XRD refinements (Fig. S2 in Supporting information) were successfully implemented using a crystallographic model of cubic pyrochlore polyantimonic acid reference (COD ID 1529908) with good reliability factors ($R_{wp} < 6\%$; $R_p < 5\%$). The typical lattice parameters for PAA-$V_{\#3}$ sample obtained by Rietveld refinement are $a = b = c = 10.276$ Å, comparatively smaller than those of PAA ($a = b = c = 10.354$ Å). Moreover, the XRD refinement results also verify that the V^{5+} ions should occupy at the 16c sites. Except for the 16c sites, the V^{5+} ions can be also assumed to position at other sites, such as 8b or 16d sites. Nevertheless, it is found that such placement led to poor convergence in the XRD refinements results (Fig. S3 in Supporting information). The results of structural analysis from XRD Rietveld refinements are summarized in Table S2 (Supporting information). Specifically, the atomic occupancy ratio of V^{5+} ions obtained from the XRD refinement can be determined to be 0.18 in PAA-$V_{\#3}$ sample.

In order to clarify the elemental composition and chemical state of the PAA-V samples, XPS was performed on PAA-$V_{\#1}$, PAA-$V_{\#3}$, and PAA-$V_{\#5}$ samples. The survey scan XPS profiles (Fig. 1c) certify the existence of Sb, V, O and C without existence of other impurities. The carbon signal comes from contamination during tests [28]. For the high-resolution Sb 3d spectrum of PAA-$V_{\#3}$ (Fig. 1d), there are two typical peaks including the one located at 540.1 eV corresponding to the Sb $3d_{3/2}$, and the other one divided into Sb $3d_{5/2}$ (531.0 eV) and O 1s (531.7 eV) [17], verifying the existence of pentavalent Sb^{5+} species. More notably, the V 2p spectrum of the PAA-$V_{\#3}$ is shown in Fig. 1e, in which two original peaks located at 516.9 and 524.2 eV correspond to the V $2p_{3/2}$ and V $2p_{1/2}$ orbitals of pentavalent V^{5+}, respectively [23]. The high-resolution XPS Sb 3d and V 2p spectra of the PAA-$V_{\#1}$ and PAA-$V_{\#5}$ are shown in Fig. S4 (Supporting information), which confirm the presence of Sb^{5+} and V^{5+} in each sample.

The morphology and microstructures of samples were revealed by FESEM and TEM characterization. Fig. S5 (Supporting information) shows the FESEM images of pristine PAA exhibiting a typical octahedron morphology with a wide size range and obvious particle agglomeration. The distribution of particle size indicates the relatively large particle size of ≈670.5 nm for the PAA. In contrast, all the as-prepared PAA-$V_{\#1\text{-}5}$ samples (Figs. 2a1 and a2, Fig. S6 in Supporting information) are mainly composed of small nanocrystals with markedly reduced particle size. Combining the FESEM images with the corresponding particle size distributions of

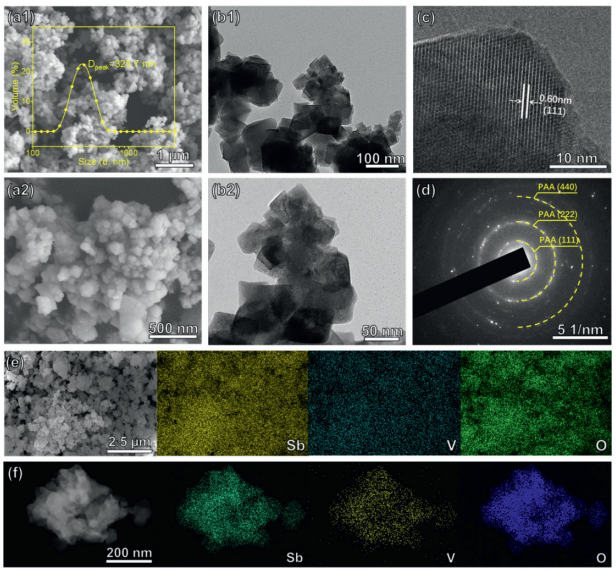

Fig. 2. (a1, a2) FESEM and (b1, b2) TEM images of the PAA-$V_{\#3}$. The inset in (a1) displays the distribution of particle size of PAA-$V_{\#3}$. (c) HRTEM image and (d) SAED pattern of the PAA-$V_{\#3}$. (e) FESEM image and the cooresponding EDX element mapping images of the PAA-$V_{\#3}$. (f) High-angle dark field scanning TEM image and cooresponding EDX element mapping images of the PAA-$V_{\#3}$.

PAA-$V_{\#1\text{-}5}$ samples, it can be observed that the PAA-$V_{\#3}$ has the best particle dispersibility with smallest average particle size of ≈325.7 nm, as compared with other samples. Besides, The particle agglomerations of PAA-$V_{\#1}$ and PAA-$V_{\#2}$ are fairly loose with mean sizes of ≈610.3 and 433.9 nm, respectively. PAA-$V_{\#4}$ and PAA-$V_{\#5}$ have tightly spherical particle agglomerations with average sizes of ≈394.5 and 609.5 nm, respectively. These results indicate that the V^{5+}-substitution could dramatically reduce the crystal size of PAA-V particles, but still keeping the pyrochlore type structure as the PAA. TEM observation was further applied to reveal microstructure of PAA-$V_{\#1}$ (Figs. S7a and b in Supporting information), PAA-$V_{\#3}$ (Figs. 2b1 and b2), and PAA-$V_{\#5}$ (Figs. S7e and f in Supporting information). Consistent with the FESEM results, the TEM images also reveal that there appear clearly particle aggregation for these samples. Especially for PAA-$V_{\#5}$, its particles seem more like sphere with above 200 nm in diameter, consisting of irregular nanoparticles. In contrast, the particles of both PAA-$V_{\#1}$ and PAA-$V_{\#3}$ present the typical octahedral morphology together with relatively smaller particle size. Nitrogen adsorption/desorption measurements were conducted to compare the porous structure and specific surface area between PAA and PAA-$V_{\#3}$ (Fig. S8 in Supporting information). The PAA-$V_{\#3}$ exhibits a BET surface area of 36.74 m^2/g with a pore volume of 0.080 cm^3/g, much higher than those of the PAA (5.06 m^2/g and 0.022 cm^3/g). Moreover, the high-resolution TEM (HRTEM) images of PAA-$V_{\#1}$ (Fig. S7c in Supporting information), PAA-$V_{\#3}$ (Fig. 2c), and PAA-$V_{\#5}$ (Fig. S7g in Supporting information) reveal the presence of clear lattice fringes with corresponding interplanar spacing of 0.61 nm, 0.60 nm, and 0.59 nm, respectively, which can be indexed to the (111) plane of the pyrochlore PAA. Notably, the interplanar spacing of the (111) plane of PAA-V samples shows a tiny decrease as the V^{5+}-substitution ratio increasing, which is consistent with above XRD results. Moreover, the selected area electron diffraction (SAED) patterns of PAA-$V_{\#1}$ (Fig. S7d in Supporting information), PAA-$V_{\#3}$ (Fig. 2d), and PAA-$V_{\#5}$ (Fig. S7h in Supporting information) also evidence their polycrystalline nature with corresponding pyrochlore phase. Note that, the SAED pattern of PAA-$V_{\#5}$ shows hazy diffraction rings, being different from that of PAA-$V_{\#1}$ and PAA-$V_{\#3}$, meaning the relatively lower crystallinity for PAA-$V_{\#5}$. This is also proved by its low strength of diffraction peaks in XRD pattern and irregular nanoparticles in TEM images. In addition, the EDX elemental mapping images of FESEM images of PAA-$V_{\#1\text{-}5}$ (Fig. 2e and Fig. S9 in Supporting information) and those of high-angle dark field scanning TEM image of PAA-$V_{\#3}$ (Fig. 2f) all prove that the Sb, V and O elements are uniformly distributed in each PAA-$V_{\#1\text{-}5}$ sample.

The contents of metal ions in the PAA-$V_{\#1\text{-}5}$ samples were measured by abovementioned EDX measurements and ICP-OES tests. The results of EDX (Fig. S10 in Supporting informaiton) and ICP-OES (Table S3 in Supporting information) indicate that the molar ratio of Sb^{5+} and V^{5+} in the five samples is as follows, 1.8:0.2 in PAA-$V_{\#1}$, 1.72:0.28 in PAA-$V_{\#2}$, 1.64:0.36 in PAA-$V_{\#3}$, 1.6:0.4 in PAA-$V_{\#4}$, and 1.6:0.4 in PAA-$V_{\#5}$, respectively. In other words, the V^{5+} replacing molar ratios of the PAA-$V_{\#1\text{-}5}$ samples are 10%, 14%, 18%, 20% and 20%, respectively. Thus, the maximum substitution ratio of V^{5+} over Sb^{5+} in PAA should be 20%, as reached in PAA-$V_{\#4}$ and PAA-$V_{\#5}$ samples, which is consistent with XRD results. Besides, the photograph of the solutions by dissolving the PAA-$V_{\#1\text{-}5}$ samples for ICP-OES tests (Fig. S11 in Supporting information) shows that color of solutions turns more and more yellow from PAA-$V_{\#1}$ to PAA-$V_{\#5}$, while the solutions of PAA-$V_{\#4}$ and PAA-$V_{\#5}$ samples exhibits the most obvious yellow color. This fact further supports the results of EDX and ICP-OES tests. Accordingly, the compositional formula of PAA-V samples could be speculated to be $(H_3O)_pH_{2-p}Sb_{2-x}V_xO6$, where $x \leq 0.4$ and the value of p detected by TG (Fig. S12a in Supporting information) in N_2 atmosphere is about 1.0. Raman spectra of the pristine PAA and PAA-$V_{\#3}$ are shown in Fig. S12b (Supporting information). They present similar Raman spectra with each other, suggesting that they share similar structure. In addition, the introduction of V^{5+} also caused the changes of peak intensities, which is consistent with previous reported Mn-substituted PAA [18].

Fig. S13a (Supporting information) visualizes the electrical conductivity and the particle size of pristine PAA and PAA-$V_{\#1\text{-}5}$. The electronic conductivity of active electrode materials directly influences the electrochemical reversibility and reaction kinetics of electrodes. Besides, the particle agglomeration state also affects the dispersion degree of active materials prepared as electrode, which determines the electrochemical performance of electrodes. In sharp contrast to the PAA with ultralow electrical conductivity of 4.9×10^{-10} S/cm, the electrical conductivity can be notably increased for all the PAA-$V_{\#1\text{-}5}$ samples. especially for the PAA-$V_{\#3}$ that has the highest electrical conductivity of 3.7×10^{-6} S/cm, almost improved by four orders of magnitude relative to the pristine PAA. Such enhanced electrical conductivity can be further reflected by the narrowed bandgap of materials, measured by UV-vis DRS technique. From the absorption spectra of PAA and PAA-$V_{\#3}$ (Fig. S13b in Supporting information), an obvious red shift phenomenon of the absorption curve from UV region to visible region can be detected after replacing the Sb^{5+} by V^{5+} in PAA, which is consistent with the color turn from white of pristine PAA to yellow of PAA-$V_{\#3}$. Based on the Kubelka-Munk equation, the energy gap of materials can be obtained from the plots of $(\alpha h\nu)^{0.5}$ *vs.* $h\nu$ (Fig. S13c in Supporting information). The bandgap value of PAA-$V_{\#3}$ is calculated to be ≈2.45 eV, much lower than that of PAA (≈3.37 eV), thus demonstrating that the V^{5+}-substitution can effectively regulate the electronic structure of PAA for significantly improving its bulk electrical conductivity and in turn favoring the electrochemical activity for lithium-ion storage.

The lithium storage performances of PAA-V as anodes materials were evaluated in coin-type half cell. The typical cyclic voltammetry (CV) curves of the PAA-$V_{\#3}$ in initial three cycles are exhibited in Fig. 3a. In the first cathodic scan, there are two apparent and wide reduction peaks. One located at ≈1.4 V can be attributed to the lithiation of PAA-$V_{\#3}$ to form Li_2O, metallic Sb and V, together with the formation of the solid electrolyte interphase (SEI) layer

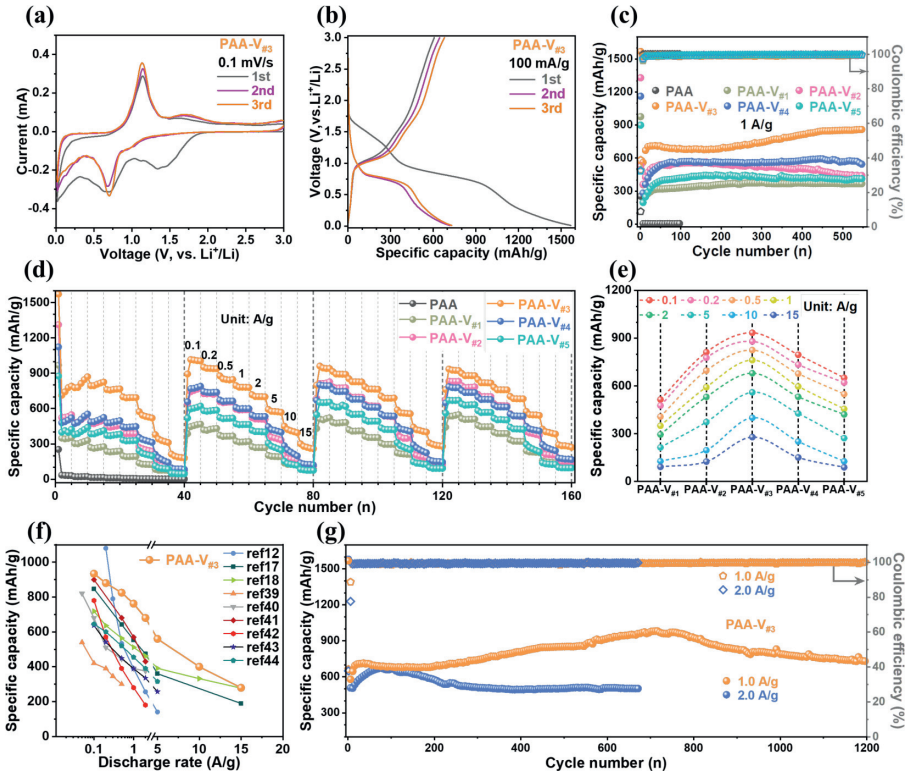

Fig. 3. (a) CV curves for the PAA-$V_{\#3}$ at a scan rate of 0.1 mV/s. (b) Initial three discharge/charge profiles of the PAA-$V_{\#3}$ at a current density of 100 mA/g. (c) Comparison of the long cycling performances of the PAA-$V_{\#1\text{-}5}$ electrodes at a current density of 1 A/g. (d) Rate performance of the PAA-$V_{\#1\text{-}5}$ electrodes. (e) Rate capabilities of the PAA-$V_{\#1\text{-}5}$ electrodes. (f) Rate capability comparison of the PAA-$V_{\#3}$ with previously reported Sb-O based anode materials. (g) Long cycling performance of the PAA-$V_{\#3}$ at 1 and 2 A/g.

[23,29]. The other at ≈0.65 V is corresponding to the alloying reaction between Sb and Li^+ forming Li_3Sb, which gradually stabilizes at 0.70 V in the second and third cycles, implying that the alloying reaction between Sb and Li^+ is highly reversible. Moreover, the peak current intensities gradually rise with the cycle number increasing, reflecting the improved electrochemical reaction activity of PAA-$V_{\#3}$ as the result of the surface/structure activation process of electrode materials accompanied with the formation of sable SEI layer [12,30–32]. In the first anodic scan, one oxidation peak appears at ≈1.14 V, which can be associated with the dealloying reaction of the Li_3Sb, and then it can be gradually fixed at 1.14 V in the following cycles with increased peak current intensities, as the same as the reduction peak at 0.70 V. Note that, an additional broad peak appears at around 1.5−1.7 V, suggesting the successive oxidation conversion reaction of metallic Sb and V. However, its low peak current intensities reflect that only a part of metallic Sb and V can be oxidized in reverse conversion reaction, which is also supported by the weak peaks at around 1.0 V in the second and third cycles of cathodic scan corresponding to reduction conversion reaction. For comparison, the CV curves of other four PAA-V samples are shown in Figs. S14a–d (Supporting information). Although they share the similar basic redox features with the PAA-$V_{\#3}$, the relatively lower peak current intensities of them indicate their relatively poorer electrochemical reaction activity than the PAA-$V_{\#3}$ electrode.

Fig. 3b presents the initial three galvanostatic discharge/charge curves of the PAA-$V_{\#3}$ at a current density of 100 mA/g between 0.01 V and 3.0 V. At the initial discharge process, there are two significant platform regions at about 1.4 and 0.65 V corresponding to the reduction conversion of PAA-V, forming metallic Sb and V and the alloying reaction to generate Li_3Sb. The platform regions at about 1.14 and 1.6 V in subsequent charge process are ascribed to the dealloying reaction and reverse oxidation conversion. These are in accordance with the CV analyses. The specific discharge/charge capacities are 1568/608 mAh/g in the first cycle, yielding a low initial Coulombic efficiency (CE) of ≈38.8%. It is worthwhile to mention that the pristine PAA presents a nearly irreversible electrochemical performance for lithium-ions storage, as previously reported by Wang *et al.* [17] and Larcher *et al.* [33]. The first three discharge/charge profiles of pristine PAA (Fig. S15 in Supporting information) display an ultralow discharge/charge specific capacities of 253/22 mAh/g with extremely poor initial CE of 8.7%. Comparatively, employing the V^{5+} to replace the Sb^{5+} in PAA is an effective approach to improving its lithium-ions storage activity and electrochemical reversibility. Moreover, the initial three discharge/charge curves of other PAA-V samples are presented in Figs. S14e–h (Supporting information), which show the similar platform regions as PAA-$V_{\#3}$, but the specific discharge/charge capacities and initial CE of them is relatively lower than those of PAA-$V_{\#3}$, which is consistent with analyses of CV measurements.

To confirm the underlying electrochemical reaction mechanism of PAA-V, *ex-situ* XRD were conducted to investigate the PAA-$V_{\#3}$ electrode. As shown in Fig. 4a, the pyrochlore structure of the PAA-$V_{\#3}$ with four typical diffraction peaks (111), (311), (222) and (400) can be clearly detected in the initial state. In the first discharge process from initial state to 1.0 V (stage A → stage C), the four characteristic diffraction peaks gradually weakened and nearly faded away, which suggests the conversion reaction of PAA-$V_{\#3}$ in this voltage range, being in accordance with the analyses of CV. In the subsequent discharge/charge process (stage D → stage G), no peaks can be detected, which could be attributed to the grain refinement of active materials with low crystallization during the electrochemical reaction. The *ex-situ* TEM technique was further applied to observe the electrochemical reactions of the PAA-$V_{\#3}$ electrode dur-

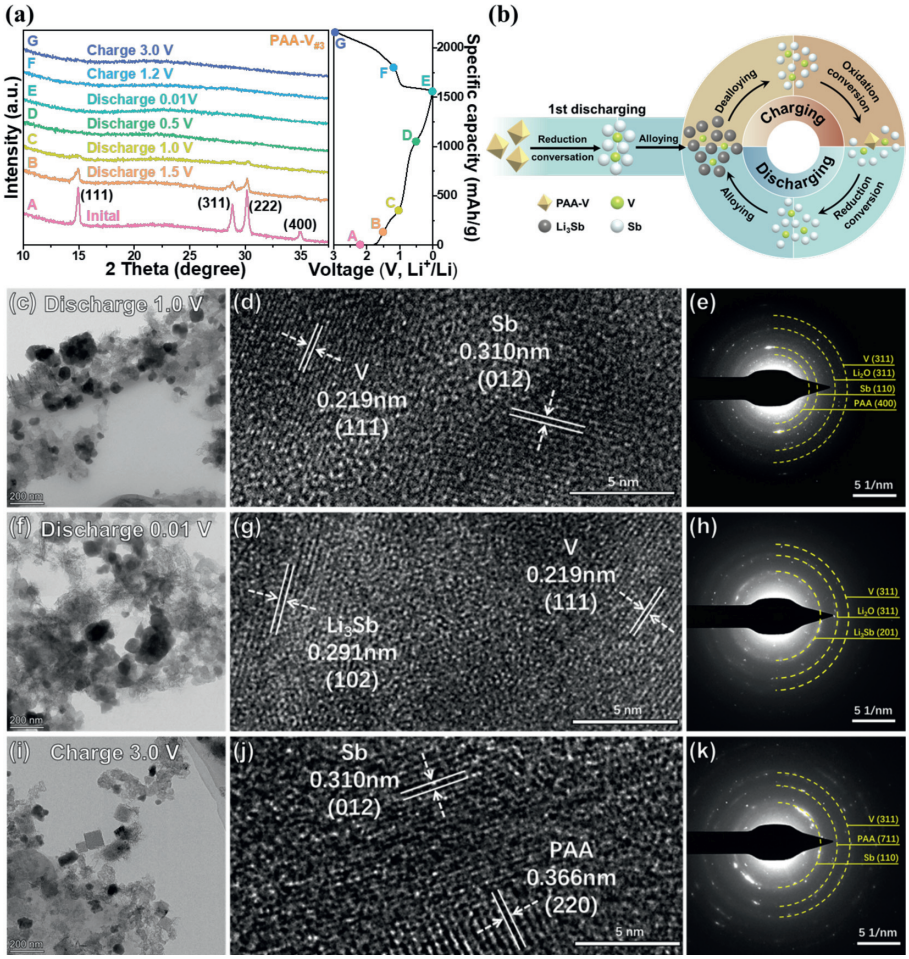

Fig. 4. (a) The *ex-situ* XRD patterns of PAA-$V_{\#3}$ at various states in the initial cycle. (b) Schematic illustation of the electrocemical reaction mechaism of PAA-V. TEM images, HRTEM images and SAED patterns of the PAA-$V_{\#3}$ electrode after discharged to (c-e) 1.0 V, (f-h) 0.01 V, and charged to (i-k) 3.0 V in the first cycle.

ing the first discharge/charge cycle. When the electrode discharge to 1.0 V (Fig. 4c), there are ultrasmall nanocrystals with irregular shape, meanwhile the lattice fringes with the interplanar spacing of 0.310 nm and 0.219 nm in the HRTEM image (Fig. 4d), corresponding to Sb (012) and V (111) planes, respectively, can be clearly discerned. Moreover, the SAED pattern in Fig. 4e reveals the coexistence of PAA phase, Li_2O, metallic Sb and V, indicating that both of Sb^{5+} and V^{5+} in the PAA-$V_{\#3}$ electrode underwent a reduction conversion into Sb^0 and V^0. After further discharged to 0.01 V (Fig. 4f), the new lattice fringes in the HRTEM image (Fig. 4g) with an interplanar distance of ≈0.291 nm is ascribed to the (102) facets of Li_3Sb, whilst none of the diffraction rings belong to metallic Sb^0 in the SAED pattern (Fig. 4h), which attributed to the full alloying reaction between Sb^0 and Li^+. It should be noted that, the lattice fringes and diffraction ring of metallic V^0 are still identified in HRTEM and SAED patterns, demonstrating that V^0 would be not involved in the alloying reaction with Li^+. The V nanocrystals retaining as metallic state, acting as *in-situ* generated conductive additives, could boost the localized electronic conductivity of the electrode. When fully charged back to 3.0 V (Figs. 4i-k), the HRTEM and SAED results reveal the disappearance of Li_3Sb and coexistence of pyrochlore structure PAA, metallic Sb and V, proving the dealloying of Li_3Sb and the partial reconstruction of PAA-V. These reactions can be also indicated by the sharp oxidation peak at ≈1.14 V and the weak one at around 1.5-1.7 V in CV patterns. Based on the above results, the electrochemical reaction mechanism of PAA-V is schematically illustrated in Fig. 4b.

The electrochemical impedance spectroscopy (EIS) measurements were carried out for the fresh cells of PAA and PAA-$V_{\#1\text{-}5}$. The measured Nyquist profiles shown in Fig. 5a were fitted by the equivalent circuit model (Fig. S16a in Supporting information). As clearly seen, the intersection of the high-frequency curved line and the horizontal axis is attributed to the electrolyte resistance (R_e) including the resistance of electrolyte, separator and the electrical contacts. The semicircle at the range of high to middle frequency is connected with the charge transfer resistance (R_{ct}) between the electrode materials and electrolyte, and the slope of the line at low frequency region is associated with the diffusion of lithium-ions inside the electrode (Warburg impedance, Z_W) [34–36]. According to the fitted results of Nyquist profiles in Table S4 (Supporting information), the R_{ct} of the PAA-$V_{\#1\text{-}5}$ electrodes are much lower than that of PAA (197.9 Ω), while the PAA-$V_{\#3}$ exhibits the lowest R_{ct} value (70.7 Ω) among them. This verifies that the introduction of V^{5+} is able to considerably enhance the kinetics of charge transportation of PAA electrodes.

The cyclic performances of the PAA-$V_{\#1\text{-}5}$ and PAA electrodes were tested at current density of 1 A/g, as shown in Fig. 3c. Except for the first cycle, the specific capacity of PAA is close to zero in the following cycles, manifesting the totally irreversibility of PAA. In sharp contrast, the PAA-$V_{\#3}$ electrode shows the best cycling stability with the highest reversible capacity remaining above 650 mAh/g over 600 cycles. Note that, the specific capacities of all the PAA-$V_{\#1\text{-}5}$ electrodes rise obviously at the beginning of cycling. Such phenomenon should be due to the special microstruc-

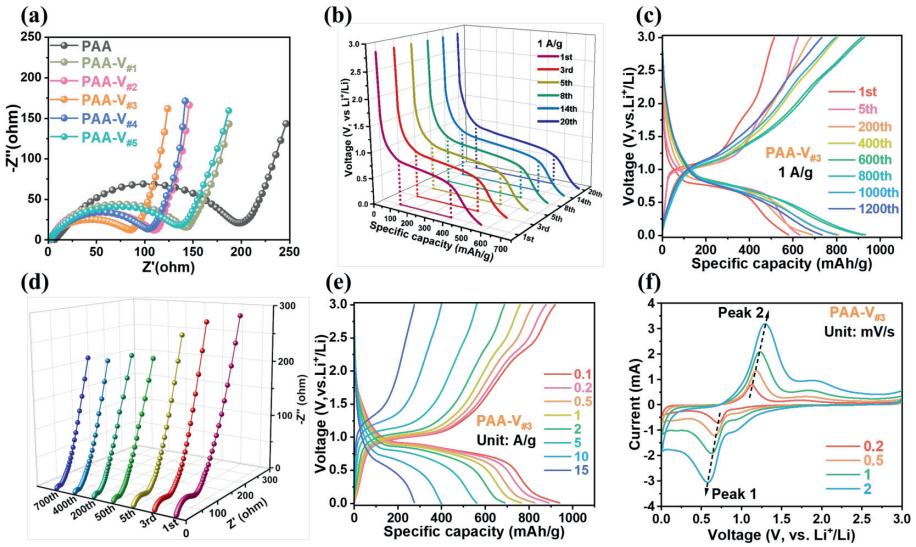

Fig. 5. (a) EIS patterns of fresh cells of PAA and PAA-$V_{\#1\text{-}5}$ electrodes. (b) Typical discharge curves of PAA-$V_{\#3}$ electrode at different cycles. (c) Discharge/charge profiles of PAA-$V_{\#3}$ for selected cycles at 1 A/g. (d) Nyquist plots of PAA-$V_{\#3}$ electrode at different cycles. (e) Discharge/charge curves of PAA-$V_{\#3}$ at different current density. (f) CV curves of PAA-$V_{\#3}$ at different scan rate.

tures of the PAA-$V_{\#1\text{-}5}$. According to the abovementioned materials characteristics, the PAA-V would occur gradual grain refinement in initial charge/discharge procsses, which could lead to exposure of more active materials and provide more active sites for Li^+ storage [37,38]. To further understand the capacity ascending phenomenon in the beginning, the selected typical discharge curves of the PAA-$V_{\#3}$ electrode at 1 A/g are shown in Fig. 5b. According to these curves, one can detect the significant capacity ascending from 561 mAh/g to 716 mAh/g in the first 20 cycles. Noteworthily, the wide discharge platform at around 0.7 V is progressively elongated, thus contributing more discharging capacity released. Moreover, the *in-situ* generated metallic V nanocrystals during the cycling are dispersed in electrode materials, which could be beneficial for enhancing the charge transfer kinetics of electrode together with boosting the lithium storage capacity. Fig. 3g shows the long-term cycling performances of PAA-$V_{\#3}$ at 1 A/g for 1200 cycles. At 1 A/g, the reversible capacity of PAA-$V_{\#3}$ electrode gradually rises to 981 mAh/g after 700 cycles and still deliver a high discharge capacity of 731 mAh/g even after 1200 cycles. Also, nearly 100% CE is observed during the whole cycling process except for the first cycle. When cycling at a higher current rate of 2 A/g, the reversible capacity maintains around 500 mAh/g until 670 cycles. Moreover, the discharge/charge curves of different cycles of PAA-$V_{\#3}$ at 1 A/g (Fig. 5c) present strong overlapping of voltage platform at ≈0.7 V in discharging process and ≈1.1 V in charging process, implying the high electrochemical reversibility of alloying reaction of Li_3Sb. To further investigate the good cycling performance of PAA-$V_{\#3}$ electrode, it was analyzed by *ex-situ* EIS technique at several selected cycles (Fig. 5d). According to the Nyquist plots and fitted results by the equivalent circuit model (Fig. S16b in Supporting information), as shown in Table S5 (Supporting information), the R_{ct} sharply declines in the initial 50 cycles, from the 1st cycle (43.5 Ω) to the 50th cycle (10.3 Ω), which is in accordance with the significant capacity ascending in the initial dozens of cycles. From the 200th to the 700th cycles, the R_{ct} of the electrode keeps at an ultralow value of ≈7 Ω, indicating the considerably enhanced charge transfer kinetics of PAA-V electrode probably due to the presence of metallic V and the grain refinement of active materials during the long cycling process. Comparing with previously reported Sb-O based anode materials, the PAA-$V_{\#3}$ developed in our work deliver a longer cycling life with a higher reversible capacity (Table S6 in Supporting information).

The rate capabilities of electrodes were investigated at various current densities from 0.1 A/g to 15 A/g, as shown in Fig. 3d. For the PAA-$V_{\#1\text{-}5}$ electrodes, the capacity ascending phenomenon also occurred in the initial cycles. Subsequently, each electrode keeps similar reversible capacity at same current density in each round, indicating that the PAA-V have good rate response and high Li^+ storage reversibility. To definitely compare the rate performances, the average rate capacities of PAA-$V_{\#1\text{-}5}$ electrodes are summarized in Fig. 3e. As shown, the PAA-$V_{\#3}$ electrode presents the best rate capacity among all the samples. When the current density reaches to 0.1, 0.2, 0.5, 1, 2 and 5 A/g, the PAA-$V_{\#3}$ can deliver high average reversible capacity of 934, 880, 825, 762, 680 and 560 mAh/g, individually. Notably, even at the ultrahigh current densities of 10 and 15 A/g, it could still achieve reversible capacity of 400 and 279 mAh/g with corresponding fast discharge/charge time of only ≈264 and 67 s, respectively. The remarkable rate capability of the PAA-$V_{\#3}$ is superior to other four PAA-V samples, as well as those of most previously reported Sb-O based anode materials (Fig. 3f) [12,17,18,39–44]. To further explicate the outstanding rate capability, the discharge/charge profiles of PAA-$V_{\#3}$ electrode at different current densities are presented in the Fig. 5e. The similar discharge/charge platforms exist at each current density, especially at ultrahigh current density of 15 A/g, suggesting the good transfer kinetics at high rates. Moreover, CV experiments at different scan rates ranging from 0.2 mV/s to 2 mV/s were applied to PAA-$V_{\#3}$ electrode (Fig. 5f). All the CV curves have a comparable shape and demonstrate a similar anodic/cathodic peak separation at different scan rates, indicating the small polarization and fast reaction kinetics of the PAA-$V_{\#3}$ electrode. In accordance with previous reports, the charge storage mechanism can be divided to two methods, that is, diffusion-controlled faradaic storage and surface-controlled *pseudo*-capacitance [45–47]. The pseudo-capacitance is contributed by the Li^+ intercalation-deintercalation reaction taking place at the near surface of active electrode materials, which is kinetically facile like capacitor. Therefore, the pseudo-capacitance can enhance the rate performance of electrode materials. These two storage ways can be characterized by following formula between the peak current (i) and scan rate (v), based on CV measurements at different

scan rates:

$$i = av^b \quad (1)$$

In the formula, a and b are parameters. The value of b can reflect the charge storage mechanism, 0.5 representing the diffusion-controlled battery process, 1 representing surface-controlled *pseudo*-capacitance, and between 0.5 and 1 presenting the hybrid mechanisms [45]. As displayed in Fig. S17a (Supporting information), the b values were obtained by plotting log(i) *versus* log(v), thus the b value of peak 1 and peak 2 are calculated to be 0.63 and 0.61, implying that the lithium-ions storage of PAA-$V_{\#3}$ electrode is a hybrid mechanism. The capacity contribution of capacitive storage can be qualified by dividing the current (i) into capacitive effects (k_1v) and diffusion-controlled insertion ($k_2v^{0.5}$) at a fixed voltage (V):

$$i(V) = k_1v + k_2v^{0.5} \quad (2)$$

Fig. S17b (Supporting information) visually exhibits the proportion of capacitive storage contribution (blue region) in the total charge storage for PAA-$V_{\#3}$ electrode at 1 mV/s, which is 64.9%. As shown in Fig. S17c (Supporting information), at the faster scan rate of 2 mV/s, the proportion of capacitive storage contribution reaches a relatively high value of 73.2%, which explains the outstanding rate performance of PAA-$V_{\#3}$ electrode. Moreover, the galvanostatic intermittent titration technique (GITT) was also employed to evaluate the lithium-ions transportation of the PAA-$V_{\#2\text{-}4}$ electrodes materials. As shown in Fig. S18 (Supporting information), the mean diffusion coefficient of lithium-ions (D_{Li^+}) in PAA-$V_{\#2\text{-}4}$ electrodes is calculated to be $\approx 3.2 \times 10^{-11}$ cm^2/s, which is nearly as high as the D_{Li^+} of some traditional cathode materials, such as $LiMn_2O_4$ ($\approx 10^{-11}$ cm^2/s) [48] and $LiCoO_2$ ($\approx 10^{-11}$ cm^2/s) [49,50], but much higher than that of $LiFePO_4$ ($\approx 10^{-14}$ cm^2/s) [51,52]. This indicates that PAA-V performs a relatively rapid transportation of lithium-ions, benefited from the unique open channels in pyrochlore crystal structure and the nano-sized particles. As shown in Figs. S19a and c (Supporting information), the thickness of PAA-$V_{\#3}$ electrode changes from 11.5 μm to 13.4 μm after 10 cycles at 1.0 A/g, thus its volume expansion is about 117%, which is an acceptable value. As shown in Figs. S19b and d (Supporting information), the PAA-$V_{\#3}$ shows smaller particles only after 10 cycles as expected. Besides, the SEI layer is formed on the electrode and remains intact without cracks.

In view of its outstanding electrochemical performance in the half cells, PAA-$V_{\#3}$ was assembled and further investigated in full lithium-ions cells by pairing commercial $LiFePO_4$ (LFP) as the cathode (Fig. 6a). The commercial $LiFePO_4$ are spherical particles with size range of 10–50 μm (Figs. S20a and b in Supporting Information). The electrochemical performance of the LFP in half cells was first evaluated in the voltage range between 2.0 V and 4.0 V. As shown in Figs. S20c and d (Supporting information), the average discharge capacity is about 154, 147, 140, 130, 123 and 113 mAh/g at current densities of 0.2, 0.5, 1, 2, 5 and 10 C (1 C = 160 mA/g), respectively, while ≈92.1% capacity retention at 1 C can be retained over 150 cycles. Given that the voltage plateaus of the LFP and PAA-$V_{\#3}$ are around 3.4 and 0.9 V (Fig. 6d), respectively, the voltage window for the corresponding full cell (PAA-$V_{\#3}$//LFP) was accordingly set in the range of 1.0–3.5 V for the following tests. In view of the typical charge/discharge profiles of the assembled PAA-$V_{\#3}$//LFP full cells, it has a high average working voltage around 2.5 V, which is high enough to power a group of commercial LEDs, as shown in the inset of Fig. 6c. The rate performance and cycling stability of the PAA-$V_{\#3}$//LFP full cells are presented in Figs. 6b and c. It should be mentioned that the N/P ratio of the tested full cells is controlled at 1.2, and thus the current density and specific capacity are calculated based on the mass of the cathode (LFP). The reversible rate capacity of the full cell at 0.2, 0.5, 1 and 2 C is about 151, 142, 132 and 118 mAh/g, respectively, being close to those of LFP in half cells, while those at high current density of 5 and 10 C can remain at 96 and 77 mAh/g, being less than those in half cells. In addition, the full cell also exhibited an outstanding cycling stability with a reversible specific capacity of 112 mAh/g at 1 C after 150 cycles (85.5% capacity retention, *vs.* the 2nd cycle). Furthermore, the discharge/charge profiles of the full cell both at varied current density (Fig. 6e) and different cycles at 1 C (Fig. 6f) exhibits a significant voltage plateau around 2.5 V, which further reflect the decent rate and cycling performance of the PAA-$V_{\#3}$//LFP full cells.

In conclusion, we successfully syntheszied V-substituted PAA materials, where the V^{5+} ions partially replace the Sb^{5+} ions in the center of SbO_6 octahedra in PAA. Such a structural regulation can decrease the size of crystals to nanoscale with reduced transportation length of Li^+ ions, and effectively modulate the electronic structure of PAA with considerably improved electrical conductivity from $\approx 10^{-10}$ S/cm to $\approx 10^{-6}$ S/cm. It is revealed that the V^{5+} components in PAA-V occur conversion reaction with Li^+

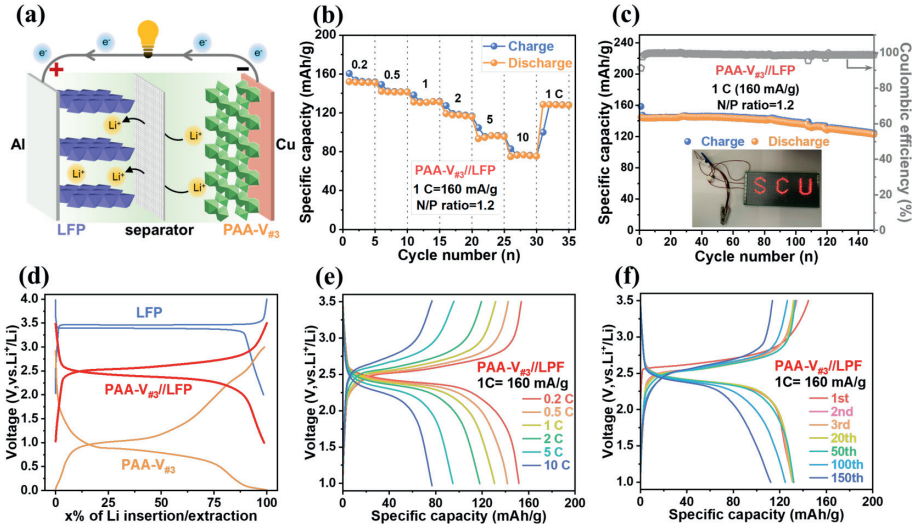

Fig. 6. (a) Schematic illustration of the PAA-$V_{\#3}$//LFP full cell. (b) Rate capability and (c) cycling performance at 1 C (= 160 mA/g) of the PAA-$V_{\#3}$//LFP full cell. The inset in (c) is the demonstration of a single coin full cell to light up red LEDs. (d) Typical charge/discharge curves of the PAA-$V_{\#3}$//LFP full cell. Typical charge/discharge profiles of the PAA-$V_{\#3}$//LFP full cell (e) at differnet current density and (f) for selected cycles at 1 C.

during charge/discharge process to *in-situ* generate metallic V^0, which can significantly boost the charge transfer kinetics of the electrodes. As such, the V^{5+}-substitution is capable to realize the PAA from totally irreversible to highly reversible for electrochemical lithium-ion storage. More importantly, when the molar ratio of V^{5+}-substitution is optimized to 18%, the fabricated PAA-V exhibits the best lithium-ion storage performance with high reversible capacity, long cycling life, excellent rate capability, and good performance in full cell application. Our work described here demonstrates an effective structural modification strategy of PAA by element substitutions for modulating its physicochemical properties toward high-performance electrochemical energy storage.

Declaration of competing interest

The authors declare that they have no known competing financial interests or personal relationships that could have appeared to influence the work reported in this paper.

Acknowledgments

The authors appreciate financial support from the National Natural Science Foundation of China (No. 21878192), the Fundamental Research Funds for the Central Universities (No. 2016SCU04A18), the 1000 Talents Program of Sichuan Province, and the Sichuan Province Science and Technology Support Program (No. 2019YFG0221). We would like to thank Lingzhu Yu from at the National Engineering Research Center for Biomaterials, Sichuan University for SEM measurements.

Supplementary materials

Supplementary material associated with this article can be found, in the online version, at doi:10.1016/j.cclet.2022.05.059.

References

[1] N. Nitta, F.X. Wu, J.T. Lee, G. Yushin, Mater. Today 18 (2015) 252–264.
[2] G. Harper, R. Sommerville, E. Kendrick, et al., Nature 575 (2019) 75–86.
[3] M. Winter, B. Barnett, K. Xu, Chem. Rev. 118 (2018) 11433–11456.
[4] M. Li, J. Lu, Z.W. Chen, K. Amine, Adv. Mater. 30 (2018) 1800561.
[5] Z.M. Liu, T. Song, U. Paik, J. Mater. Chem. A 6 (2018) 8159–8193.
[6] J. He, Y.Q. Wei, T.Y. Zhai, H.Q. Li, Mat. Chem. Front. 2 (2018) 437–455.
[7] L.Y. Kovalenko, V.A. Burmistrov, A.A. Biryukova, Russ. J. Electrochem. 52 (2016) 694–698.
[8] L.H. Baetsle, D. Huys, J. Inorg, Nucl. Chem. 30 (1968) 639–649.
[9] T.N. Yu, H.B. Zhang, H.Z. Cao, G.Q. Zheng, Chem. Eng. J. 360 (2019) 313–324.
[10] F. Girardi, E. Sabbioni, J. Radioanal. Chem. 1 (1968) 169–178.
[11] Y.M. Tan, L.J. Chen, H. Chen, Q.L. Hou, X.H. Chen, Mater. Lett. 212 (2018) 103–106.
[12] X.Z. Zhou, Z.F. Zhang, X.H. Xu, et al., ACS Appl. Mater. Interfaces 8 (2016) 35398–35406.
[13] C.Z. Ke, F. Liu, Z.M. Zheng, et al., Rare Met. 40 (2021) 1347–1356.
[14] X.Y. Feng, H.H. Wu, B. Gao, et al., Nano Res. 15 (2022) 352–360.
[15] M. Cai, H. Zhang, Y. Zhang, et al., Sci. Bull. 67 (2022) 933–945.
[16] F. Ni, Y. Ma, J. Chen, W. Luo, J. Yang, Chin. Chem. Lett. 32 (2021) 2073–2078.
[17] B.Y. Wang, Z.W. Deng, Y.T. Xia, et al., Adv. Energy Mater. 10 (2020) 1903119.
[18] B.Y. Wang, Y.H. Wei, H.Y. Fang, et al., Adv. Sci. 8 (2021) 2002866.
[19] H.D. Zhou, C.R. Wiebe, J.A. Janik, et al., J. Solid State Chem. 183 (2010) 890–894.
[20] K. Ozawa, M. Hase, H. Fujii, et al., Electrochim. Acta 50 (2005) 3205–3209.
[21] Y.Q. Jia, J. Solid State Chem. 95 (1991) 184–187.
[22] J. Morales, L. Sanchez, F. Martin, F. Berry, J. Solid State Chem. 179 (2006) 2554–2561.
[23] Y.T. Hao, Y. Jiang, L.Z. Zhao, et al., ACS Appl. Mater. Interfaces 13 (2021) 21127–21137.
[24] N.N. Wang, Z.C. Bai, Y.T. Qian, J. Yang, Adv. Mater. 28 (2016) 4126–4133.
[25] X.M. Kang, G.D. Fu, X.W. Wang, et al., Chin. Chem. Lett. 32 (2021) 938–942.
[26] W.A. England, M.G. Cross, A. Hamnett, P.J. Wiseman, J.B. Goodenough, Solid State Ion. 1 (1980) 231–249.
[27] R.C.T. Slade, G.P. Hall, A. Ramanan, E. Prince, Solid State Ion. 92 (1996) 171–181.
[28] Z.J. Zhang, H.L. Zhao, Y.Q. Teng, et al., Adv. Energy Mater. 8 (2018) 1700174.
[29] Y.T. Yan, X.L. Zhao, H.L. Dou, et al., Chin. Chem. Lett. 32 (2021) 910–913.
[30] C. Chen, Q. Liang, G. Wang, D. Liu, X. Xiong, Adv. Funct. Mater. 32 (2022) 2107249.
[31] Q.K. Zhang, X.Q. Zhang, H. Yuan, J.Q. Huang, Small Sci. 1 (2021) 2100058.
[32] C. Chen, Q. Liang, Z. Chen, et al., Angew. Chem. Int. Ed. 133 (2021) 26922–26928.
[33] D. Larcher, A.S. Prakash, L. Laffont, et al., J. Electrochem. Soc. 153 (2006) A1778–A1787.
[34] C.R. Hao, T.G. Gao, A.B. Yuan, J.Q. Xu, Chin. Chem. Lett. 32 (2021) 113–118.
[35] G. Zhu, R. Guo, W. Luo, et al., Natl. Sci. Rev. 8 (2021) nwaa152.
[36] F.Z. Zhang, Y.Y. Ma, M.M. Jiang, W. Luo, J.P. Yang, Rare Met. 41 (2022) 1276–1283.
[37] P. Jing, Q. Wang, B.Y. Wang, et al., Ceram. Int. 45 (2019) 216–224.
[38] C.P. Wang, J.T. Yan, T.Y. Li, et al., Angew. Chem. Int. Ed. 60 (2021) 25013–25019.
[39] Y. Liu, H.C. Wang, K.K. Yang, et al., Appl. Sci. 9 (2019) 2677.
[40] O.A. Jaramillo-Quintero, M. Benitez-Cruz, J.L. Garcia-Ocampo, A. Cano, M.E. Rincon, J. Alloy. Compd. 807 (2019) 151647.
[41] M.X. Deng, S.J. Li, W.W. Hong, et al., Mater. Chem. Phys. 223 (2019) 46–52.
[42] Q.G. Han, Y.B. Sun, W.Q. Zhang, et al., Ionics 26 (2020) 1221–1228.
[43] Y. Li, Z.J. Song, T.T. Sun, et al., Int. J. Hydrog. Energy 46 (2021) 26308–26317.
[44] C. Xian, W. Liang, M. Feng, et al., Nanoscale Adv. 2 (2020) 5578–5583.
[45] J.L. Liu, J. Wang, C.H. Xu, et al., Adv. Sci. 5 (2018) 1700322.
[46] N.T. Wu, J.K. Shen, L. Sun, et al., Electrochim. Acta 310 (2019) 70–77.
[47] N.T. Wu, W.D. Tian, J.K. Shen, et al., Inorg. Chem. Front. 6 (2019) 192–198.
[48] S.B. Tang, M.O. Lai, L. Lu, Mater. Chem. Phys. 111 (2008) 149–153.
[49] Q. Liu, X. Su, D. Lei, et al., Nat. Energy 3 (2018) 936–943.
[50] J. Xie, N. Imanishi, T. Matsumura, et al., Solid State Ion. 179 (2008) 362–370.
[51] B.Y. Wang, Y. Wang, H. Wu, et al., ChemElectroChem 4 (2017) 1141–1147.
[52] K. Tang, X.Q. Yu, J.P. Sun, H. Li, X.J. Huang, Electrochim. Acta 56 (2011) 4869–4875.